

1 **GPU-based finite-size pencil beam algorithm with 3D-**  
2 **density correction for radiotherapy dose calculation**

3 **Xuejun Gu<sup>1</sup>, Urszula Jelen<sup>2</sup>, Jinsheng Li<sup>3</sup>, Xun Jia<sup>1</sup>, and Steve B. Jiang<sup>1</sup>**

4  
5 <sup>1</sup>Center for Advanced Radiotherapy Technologies and Department of Radiation  
6 Oncology, University of California San Diego, La Jolla, CA 92037-0843, USA

7 <sup>2</sup>University Hospital Giessen and Marburg, Department of Radiotherapy and  
8 Radiation Oncology, Particle Therapy Center Marburg, 34045 Marburg,  
9 Germany

10 <sup>3</sup>Department of Radiation Oncology, Fox Chase Cancer Center, 333 Cottman  
11 Avenue, Philadelphia, PA 19111, USA

12  
13 E-mail: sbjiang@ucsd.edu

14  
15 Targeting at the development of an accurate and efficient dose calculation  
16 engine for online adaptive radiotherapy, we have implemented a finite size  
17 pencil beam (FSPB) algorithm with a 3D-density correction method on GPU.  
18 This new GPU-based dose engine is built on our previously published ultrafast  
19 FSPB computational framework [Gu et al. *Phys. Med. Biol.* **54** 6287-97, 2009].  
20 Dosimetric evaluations against Monte Carlo dose calculations are conducted on  
21 10 IMRT treatment plans (5 head-and-neck cases and 5 lung cases). For all  
22 cases, there is improvement with the 3D-density correction over the  
23 conventional FSPB algorithm and for most cases the improvement is significant.  
24 Regarding the efficiency, because of the appropriate arrangement of memory  
25 access and the usage of GPU intrinsic functions, the dose calculation for an  
26 IMRT plan can be accomplished well within 1 second (except for one case) with  
27 this new GPU-based FSPB algorithm. Compared to the previous GPU-based  
28 FSPB algorithm without 3D-density correction, this new algorithm, though  
29 slightly sacrificing the computational efficiency (~5-15% lower), has  
30 significantly improved the dose calculation accuracy, making it more suitable  
31 for online IMRT replanning.

32  
33 Submitted to *Physics in Medicine and Biology*

## 34 **1. Introduction**

35

36 Online adaptive radiotherapy (ART) appears to be attractive, as it allows real-time  
37 adaptation of the treatment to daily anatomical variations (Wu *et al.*, 2002; Wu *et al.*,  
38 2004; Court *et al.*, 2005; Mohan *et al.*, 2005; Court *et al.*, 2006; Wu *et al.*, 2008; Lu *et*  
39 *al.*, 2008; Ahunbay *et al.*, 2008; Fu *et al.*, 2009; Godley *et al.*, 2009; Men *et al.*, 2009; Gu  
40 *et al.*, 2009; Gu *et al.*, 2010b; Men *et al.*, 2010a; Men *et al.*, 2010b; Ahunbay *et al.*,  
41 2010). However, it is challenging to implement online ART in clinical practice due to  
42 various technical barriers. One major barrier is to accurately compute dose distribution on  
43 the patient's new geometry in real time. Recently, a massive parallel computing  
44 architecture, graphics processing unit (GPU), has been introduced into the radiotherapy  
45 community and applied to accelerate computationally intensive tasks (Sharp *et al.*, 2007;  
46 Yan *et al.*, 2007; Li *et al.*, 2008; Samant *et al.*, 2008; Men *et al.*, 2009; Gu *et al.*, 2010b;  
47 Men *et al.*, 2010a; Men *et al.*, 2010b; Lu, 2010; Lu and Chen, 2010; Jia *et al.*, 2010b).  
48 Much effort has been devoted to utilize GPU to speed up dose calculation algorithms,  
49 including Monte Carlo (MC) simulation, superposition/convolution (S/C), and finite size  
50 pencil beam (FSPB) (Hissoiny *et al.*, 2009; Gu *et al.*, 2009; Jia *et al.*, 2010a; Jacques *et*  
51 *al.*, 2010; Hissoiny *et al.*, 2010).

52 The GPU-based FSPB model developed by our group is capable of calculating the  
53 dose distribution for a 9-field prostate treatment plan within 1 second (Gu *et al.*, 2009).  
54 However, like any other conventional FSPB models, our model only accounts for 1D  
55 density correction along the pencil beam depth direction and thus is less accurate when  
56 major inhomogeneities exist such as in lung cancer and head-and-neck cancer cases.  
57 Jelen and Alber (2007) have proposed a 3D density correction approach to improve the  
58 accuracy of an FSPB model (Jelen *et al.*, 2005). This improved FSPB model, termed as  
59 the *DC-FSPB* model in this paper, provides both lateral and longitudinal density  
60 corrections. Using a single flat  $10 \times 10\text{cm}^2$  beam in a lung case and a  $6 \times 6\text{cm}^2$  beam  
61 in a head-and-neck case, the authors initially demonstrated the accuracy of the model to  
62 be better than 2% for the majority of the voxels inside the field, which is a great  
63 improvement over the conventional FSPB models. In this paper, we will focus the  
64 implementation of this DC-FSPB model on GPU and exam its accuracy and efficiency  
65 using real clinical IMRT cases. We will 1) incorporate the DC-FSPB model into our  
66 GPU-based FSPB dose calculation framework; 2) systematically evaluate and  
67 demonstrate the accuracy improvement of the GPU-based DC-FSPB algorithm (*g-DC-*  
68 *FSPB*) over the GPU-based conventional FSPB algorithm (*g-FSPB*) under clinically  
69 realistic situations; 3) analyze in detail the ability of the *g-DC-FSPB* algorithm in  
70 handling various inhomogeneity situations; and 4) assess the efficiency of the *g-DC-*  
71 *FSPB* algorithm in comparison with the *g-FSPB* algorithm.

72

## 73 **2. Methods and Materials**

74

### 75 *2.1 An FSPB model with 3D density correction (DC-FSPB)*

76

77 In the DC-FSPB model proposed by Jelen and Alber (2007), the coefficients of the pencil  
 78 beam kernel were commissioned using the XVMC Monte Carlo simulation results  
 79 (Fippel *et al.*, 1999) in a homogenous water phantom and in a heterogeneous phantom  
 80 with slab geometry. Briefly, the dose at a spatial point  $\mathbf{r}$  is the summation of the  
 81 contributions from all beamlets:

$$D(\mathbf{r}) = \sum D_i(\mathbf{r}) f_i, \quad (1)$$

82 where  $f_i$  denotes the photon fluence (or beamlet intensity) for the beamlet  $i$ . The dose  
 83 distribution of the beamlet  $i$  with unit intensity from a point source located at  $\mathbf{r}_s$  can be  
 84 formulated as:

$$D_i(\mathbf{r}) = F(x, y, \omega(\rho, t), u_x(\rho, t), u_y(\rho, t), x_0, y_0) \cdot A(t_{eq}, \theta) \cdot \left(\frac{SAD}{|\mathbf{r}_a|}\right)^2. \quad (2)$$

85 Here,  $\mathbf{r}_a$  denotes the projection of the vector  $\mathbf{r} - \mathbf{r}_s$  onto the beamlet direction.  $x, y$  are  
 86 the projections of the vector  $\mathbf{r} - \mathbf{r}_s - \mathbf{r}_a$  onto  $x$ -axis and  $y$ -axis of the plane perpendicular  
 87 to the beamlet direction.  $x_0$  and  $y_0$  represent the beamlet size.  $x, y, x_0$ , and  $y_0$  are defined  
 88 at the isocenter plane.  $SAD$  is the source to axis distance.  $t$  is the portion of  $|\mathbf{r}_a|$  below the  
 89 surface and  $t_{eq}$  is the radiological depth.  $\theta$  is the angle between the beamlet and its  
 90 corresponding beam central axis.  $\omega$ 's denote weighting factors and  $u$ 's are the steepness  
 91 parameters of the beam's penumbra. The function  $F$  is the summation of two terms,  
 92 formulated as

$$F(x, y, \omega, u_x, u_y, x_0, y_0) = \sum_{i=1}^2 \omega_i p(x, u_{ix}, x_0) p(y, u_{iy}, y_0). \quad (3)$$

93 Here, one term models the primary dose and the other one represents the secondary dose  
 94 accounting for scattering components. Each term is a product of two independent  
 95 exponential functions. Specifically  $p(x, u_{ix}, x_0)$  is defined as:

$$p(x, u_{ix}, x_0) = \begin{cases} \sinh(u_{ix} x_0) \exp(u_{ix} x) & \text{for } x < -x_0 \\ 1 - \cosh(u_{ix} x) \exp(-u_{ix} x_0) & \text{for } -x_0 \leq x \leq x_0 \\ \sinh(u_{ix} x_0) \exp(-u_{ix} x) & \text{for } x > x_0 \end{cases} \quad (4)$$

96 The term for  $p(y, u_{iy}, y_0)$  is similarly defined. By adjusting the parameters in Eqs. (2)-  
 97 (4), we are able to shape the beamlet dose distribution in three dimensions. Along the  
 98 beamlet direction,  $A(t_{eq}, \theta)$  is a function of radiological depth and off-axis angle, taking  
 99 care of heterogeneity correction along beamlet depth direction as well as the horn effect  
 100 at various off-axis distances. Perpendicular to the beamlet direction, the beam's  
 101 penumbra steepness is tuned according to local density  $\rho$  as  $u_1(\rho, t) = f_{u_1}(\rho) \cdot u_1^w(t)$   
 102 and a smoothed density  $\hat{\rho}$  as  $u_2(\rho, t) = f_{u_2}(\hat{\rho}) \cdot u_2^w(t)$ , where the smoothed density  $\hat{\rho}$  is  
 103 obtained by convolving the local density  $\rho$  with a 3D symmetric Gaussian kernel. Here,  
 104  $u_1^w(t)$  and  $u_2^w(t)$  are the parameters commissioned in a homogenous water phantom at a  
 105 geometrical depth  $t$  and  $f_{u_1}(\rho)$  and  $f_{u_2}(\hat{\rho})$  are penumbra widening factors. The  
 106 weighting factors  $\omega_i$  adjust the proportions of primary and secondary dose according to  
 107 the smoothed density  $\hat{\rho}$  and the beamlet passing history using a formula  $\omega_i(\rho, t) =$   
 108  $f_{\omega_i}(\hat{\rho}) \cdot (\omega_i^w(t) + \omega_i^{corr}(t))$ , where  $f_{\omega_i}(\hat{\rho})$  adjusts weighting factors locally according  
 109 to a smoothed density  $\hat{\rho}$ .  $\omega_i^w(t)$  is the commissioned weighting factor in a homogenous  
 110 water phantom at a depth  $t$ .  $\omega_i^{corr}(t) = \int_0^t b(\rho(t')) dt'$ , where  $b(\rho(t'))$  is a parameter

111 describing the changing of  $\omega_i(\rho, t)$  values with the existence of heterogeneities. The  
 112 details of the DC-FSPB model can be found in the reference (Jelen and Alber, 2007).

113 In this work, the model parameters were commissioned for the 6MV beam of a  
 114 Varian 21EX linac using Monte Carlo simulated dose distributions. The dose  
 115 distributions were calculated using the MCSIM Monte Carlo code (Ma *et al.*, 2002)  
 116 together with a realistic source model (Jiang *et al.*, 2000) for a  $10 \times 10 \text{ cm}^2$  field with  
 117 SAD=100 cm and SSD=90 cm. A slab geometry phantom of  $30 \times 30 \times 30 \text{ cm}^3$   
 118 dimension was used for commissioning. The slab of 15 cm thickness is inserted at 8cm  
 119 below the phantom surface with the density varying from 0.1 to  $2.0 \text{ g/cm}^3$ . The  
 120 parameters in the DC-FSPB model, such as  $u$ ,  $\omega$ ,  $f(\cdot)$ , and  $b(\cdot)$ , were obtained by fitting  
 121 the dose distributions of the DC-FSPB model to those of the MCSIM simulation.

122 Once the parameters are established, the dose distribution for a board beam can be  
 123 calculated using Eq. (1). Algorithm A1 given below illustrates the CPU implementation  
 124 of the DC-FSPB algorithm. It, if skipping step 11, is degenerated to the FSPB algorithm  
 125 with longitudinal density correction only.

126 **Algorithm A1:** An FSPB algorithm with 3D density correction implemented on CPU  
 127 (DC-FSPB).

- 
- 128
- 129 1. Calculate a smoothed density distribution  $\hat{\rho}$  by convolving the density  
 130 distribution  $\rho$  from patient CT data with a spherical Gaussian kernel;
  - 131 2. For each beamlet:
    - 132 3. Calculate the beamlet angle  $\theta$ ;
    - 133 4. Extract the beamlet entrance and exit points on patient's body surface;
    - 134 5. Build a lookup table for radiological depth  $t_{eq} = \int_0^t \frac{\mu(t')}{\mu_{H_2O}} dt'$ ;
    - 135 6. Build a lookup table for the weighting factor correction term:  
 136 
$$\omega_i^{corr}(t) = \int_0^t b(\rho(t')) dt'$$
;
    - 137 7. For each voxel:
      - 138 8. For each beamlet such that the voxel is inside the region of interest  
 139 (ROI)\* of the beamlet
      - 140 9. Extract  $A(t_{eq}, \theta)$  from the commissioned parameter lookup table;
      - 141 10. Extract  $u_i^W(t)$  and  $\omega_i^W(t)$  from the commissioned parameter lookup  
 142 table;
      - 143 11. Calculate density corrected parameters:  
 144 
$$u_1(\rho, t) = f_1(\rho)u_1^W(t);$$
  
 145 
$$u_2(\rho, t) = f_2(\hat{\rho})u_2^W(t);$$
  
 146 
$$\omega_i(\rho, t) = \omega_i^W(t) + \omega_i^{corr}(t);$$
      - 147 12. Calculate the dose according to Eqs. (1) and (2);
      - 148 13. End For
      - 149 14. End For
      - 150 15. End For
-

152 \*Here, ROI is defined as a cylinder of a radius of 5 cm centered at the beamlet  
 153 central axis.

154

## 155 2.2 GPU implementation

156

157 Algorithm A2 is the GPU implementation of Algorithm A1 using Compute Unified  
 158 Device Architecture (CUDA) programming environment. Similar to the CPU algorithm,  
 159 in Kernel 5, if we skip the density correction calculations, the g-DC-FSPB algorithm is  
 160 degenerated to the g-FSPB algorithm.

161 **Algorithm A2:** An FSPB algorithm with 3D density correction implemented on GPU  
 162 (g-DC-FSPB).

163

- 
- 164 1. Transfer the beam setup parameters, patient CT data, and commissioned model  
 165 parameters from CPU to GPU;
  - 166 2. Kernel 1: Perform an convolution to obtain smoothed density distribution  $\hat{\rho}$  in  
 167 parallel (Step 1 in Algorithm A1);
  - 168 3. Kernel 2: Calculate the beamlet angle  $\theta$  for all beamlets in parallel (Step 3 in  
 169 Algorithm A1);
  - 170 4. Kernel 3: Extract the beamlet entrance and exit points on the patient's body  
 171 surface for beamlets in parallel (Step 4 in Algorithm A1);
  - 172 5. Kernel 4: Build a radiological depth lookup table and a weighting factor  
 173 correction lookup table for all beamlets in parallel (Steps 5-6 in Algorithm A1);
  - 174 6. Kernel 5: Calculate dose to all voxels in parallel for all the beamlets (Steps 7-14  
 175 in Algorithm A1);
  - 176 7. Transfer the dose distribution from GPU to CPU.
- 

177

178 The efficiency of a GPU code heavily relies on the efficiency of the memory  
 179 management. On a GPU card, available memory consists of constant memory, global  
 180 memory, shared memory, and texture memory. The constant memory is cached, which  
 181 requires only one memory instruction (4 clock cycles) to access. However, the available  
 182 constant memory is limited to 64 kB on a typical GPU card (such as NVIDIA Tesla  
 183 C1060). Due to the limited space, we store only those frequently accessed arrays with  
 184 constant values in the constant memory, such as the beam setup parameters and the  
 185 commissioned model parameters. The global memory is not cached and requires  
 186 coalesced memory access to achieve an optimal usage, but it has a large capacity (4GB  
 187 on one Tesla C1060 card) and is writable. Thus, we assign the radiological depth array  
 188 and the dose distribution array in the global memory since they requires memory writing.  
 189 The texture memory is read-only memory, but it is cached and the texture fetch are not  
 190 restricted by the coalescing memory access pattern to achieve high performance. The  
 191 density array is rested in the texture memory. By doing so, the performance is improved  
 192 with texture fetching in Kernel 1 and Kernel 4, where the convolution and integration  
 193 cannot follow the global memory coalescing accessing requirement.

194 The radiological depth and the weighting factor correction calculations require the  
 195 integration of the density functions along the beamlet direction, which is a  
 196 computationally intensive ray tracing problem. Siddon’s algorithm is commonly used on  
 197 most CPU platforms for this task (Siddon, 1985). However, with Siddon’s algorithm,  
 198 since the segment length that the beamlet central-axis intersects with each voxel is not  
 199 constant, the lookup table of the radiological depth (or the weighting factor correction  
 200 term) for each beamlet has to include two arrays: one storing the radiological depth (or  
 201 the weighting factor correction term) while the other auxiliary array listing the  
 202 corresponding geometrical depth. In Kernel 5 of Algorithm A2, for each voxel, we have  
 203 to search the geometrical depth array and then calculate the corresponding radiological  
 204 depth (or weighting factor). In order to reduce the memory usage and improve the  
 205 efficiency, in this work we adopt another approach to avoid the storage and search of the  
 206 geometrical depth auxiliary array. This approach computes the radiological depth and the  
 207 weighting factor correction term at the sampling points uniformly distributed along the  
 208 beamlet central-axis. The sampling step size is chosen as  $d = \frac{1}{2} \min(\delta_x, \delta_y, \delta_z)$ ,  
 209 where  $\delta_x, \delta_y, \delta_z$  represent the voxel size in  $x, y$  and  $z$  dimension. With this approach,  
 210 the storing and searching of the geometrical depth array becomes unnecessary. The  
 211 involved interpolation procedures can be conducted with high efficiency using the fast  
 212 on-chip linear interpolation function.

213 We compute the hyperbolic and exponential functions in Eq. (4) using CUDA  
 214 intrinsic function `_expf(z)`, which is about an order of magnitude faster than the standard  
 215 math function `expf(z)`. The maximum ulp (unit of least precision) error of `_expf(z)` is  
 216 bounded by  $2 + \text{floor}(\text{abs}(1.16 * z))$  (NVIDIA, 2010). For the data used in our g-DC-  
 217 FSPB model, since  $z < 0.5$  the error of function `_expf(z)` is actually bounded by 2  
 218 maximum ulp, which is equal to the error of the function `expf(z)`. Therefore, the use of  
 219 the intrinsic function `_expf(z)` can greatly increase the efficiency without losing any  
 220 accuracy.

221

### 222 2.3 Evaluation

223

**Table 1.** Tumor site, number of beams, and case dimension for 5 head-and-neck (H1-H5) cases and 5 lung (L1-L5) cases.

Case	Tumor Site	# of Beams	# of Beamlets	# of Voxels
H1	Parotid	8 (non-coplanar)	7,264	128×128×72
H2	Hypopharynx	7 (non-coplanar)	4,429	128×128×72
H3	Nasal Cavity	8 (non-coplanar)	3,381	128×128×72
H4	Parotid	5 (coplanar)	4,179	128×128×72
H5	Larynx	7 (non-coplanar)	10,369	128×128×72
L1	Left lung, low lobe(close to pleura)	6 (coplanar)	637	128×128×80
L2	Right lung, low lobe (paravertebral)	6 (coplanar)	1,720	128×128×103
L3	Left lung, upper lobe (close to pleura)	5 (coplanar)	921	128×128×80
L4	Right lung, upper lobe (close to heart)	7 (coplanar)	841	128×128×80
L5	Left lung (middle)	5 (coplanar)	686	128×128×80

224 The g-DC-FSPB algorithm was evaluated for its accuracy against MCSIM algorithm (Ma  
 225 *et al.*, 2002) and its efficiency using 10 real IMRT plans: 5 head-and-neck (H1-H5) cases  
 226 and 5 lung (L1-L5) cases. All treatment plans were initially generated on the Eclipse  
 227 planning system (Eclipse, Varian Medical Systems, Inc. Palo Alto, CA) and used to treat  
 228 patients. Table 1 lists some relevant information for these 10 evaluation cases. The  
 229 original CT images were down-sampled to the resolution of  $0.4 \times 0.4 \times 0.25\text{cm}^3$  for the  
 230 dose calculations using MCSIM, g-FSPB, and g-DC-FSPB codes. Treatment plan  
 231 parameters, including beam setup, leaf sequences, monitor units, *etc.*, were extracted  
 232 from the Eclipse planning system and converted into RTP files as the input for MCSIM  
 233 dose calculation. Leaf sequences and monitor units were reformatted into fluence map  
 234 files as the input of g-FSPB and g-DC-FSPB codes. The resolution of the fluence maps  
 235 (or the beamlet size) was selected as  $0.2 \times 0.5\text{cm}^2$  with 0.2 cm along the MLC leaf  
 236 motion direction.

237 For accuracy evaluation, the dose distributions calculated with MCSIM were used as  
 238 the ground truth, with the maximum relative uncertainty less than 0.1% by simulating 2  
 239 billion particles for each beam. We computed the absolute dose in cGy for both g-DC-  
 240 FSPB and MCSIM. The 3D  $\gamma$ -index distributions were computed using a GPU-based  
 241 algorithm (Gu *et al.*). Dose distributions were evaluated with 3%-3mm criteria, where the  
 242 3% is relative to the maximum MCSIM dose value ( $D_{max}$ ). The following statistical  
 243 parameters were calculated and used as metrics to evaluate the dose calculation accuracy:  
 244 1)  $\gamma^{max}$ : the maximum  $\gamma$  value of the entire dose distribution; 2)  $\gamma_{50}^{avg}$ : the average  $\gamma$   
 245 values inside 50% isodose lines; 3)  $P_{50}$ : the percentage of voxels inside 50% isodose  
 246 lines with  $\gamma < 1.0$ . For the efficiency evaluation, both g-FSPB and g-DC-FSPB dose  
 247 calculations were conducted on an NVIDIA Tesla C1060 card. The data transferring time  
 248 and the GPU computation time were recorded separately.

249

### 250 3. Results and Discussion

251

#### 252 3.1 Accuracy evaluation

253

##### 254 3.1.1 Head-and-neck cases

255

**Table 2.** Gamma index evaluation results for 5 head-and-neck cases using the g-DC-FSPB algorithm. The corresponding g-FSPB results are given in parenthesis for comparison purpose.

Case #	$\gamma^{max}$	$\gamma_{50}^{avg}$	$P_{50}$
H1	2.12 (2.16)	0.30 (0.31)	97.53% (97.32%)
H2	3.44 (4.11)	0.28 (0.28)	97.80% (97.01%)
H3	2.27 (2.36)	0.46 (0.52)	92.29% (86.39%)
H4	3.08 (3.11)	0.61 (0.63)	82.96% (81.56%)
H5	3.33 (3.37)	0.61 (0.61)	86.19% (86.09%)

256

257 Table 2 summarizes the  $\gamma$ -index evaluation results for 5 head-and-neck cases. We can see  
 258 that, for all 5 cases,  $\gamma^{max}$  and  $\gamma_{50}^{avg}$  values are smaller and  $P_{50}$  values are larger for the g-

259 DC-FSPB algorithm, indicating that the new algorithm with 3D density correction  
 260 constantly outperforms the conventional FSPB algorithm. Specifically, we can put these  
 261 five cases into three scenarios:

262 *Scenario 1 (Case H1 and Case H2) - both g-FSPB and g-DC-FSPB algorithms are*  
 263 *accurate.* For these two cases, the average  $\gamma$ -index values are low ( $\sim 0.3$ ) and the passing  
 264 rates are high ( $>97\%$ ) for both the g-FSPB and g-DC-FSPB algorithms. By closely  
 265 inspecting the patient geometries and the treatment plans for Cases H1 and H2, we found  
 266 that there are only minor inhomogeneities on beams' paths and thus the g-FSPB  
 267 algorithm can calculate the dose distributions quite accurately. In such cases, there is not  
 268 much room for the g-DC-FSPB algorithm to improve the accuracy.

269 *Scenario 2 (Case H3) - the g-FSPB algorithm is less accurate but the g-DC-FSPB*  
 270 *algorithm can greatly improve the accuracy.* Figures 1(a), (b) and (c) show the dose  
 271 distributions for Case H3 calculated with the MCSIM, g-FSPB, and g-DC-FSPB  
 272 algorithms in the XY plane through isocenter, respectively. The  $\gamma$ -index distributions in  
 273 the same plane are presented in Figures 1(d) and (e), from which we can see that the  $\gamma$ -  
 274 index values decrease significantly at the nasal cavity region when the 3D density  
 275 correction is applied. The statistical analysis of the  $\gamma$ -index also shows that the g-DC-  
 276 FSPB dose distribution has a lower average  $\gamma$ -index value and a higher passing rate  
 277 compared to the g-FSPB result. These results indicate that the g-DC-FSPB algorithm is  
 278 capable of calculating dose more accurately in a low-density region (*e.g.* nasal cavity)  
 279 than the g-FSPB algorithm.

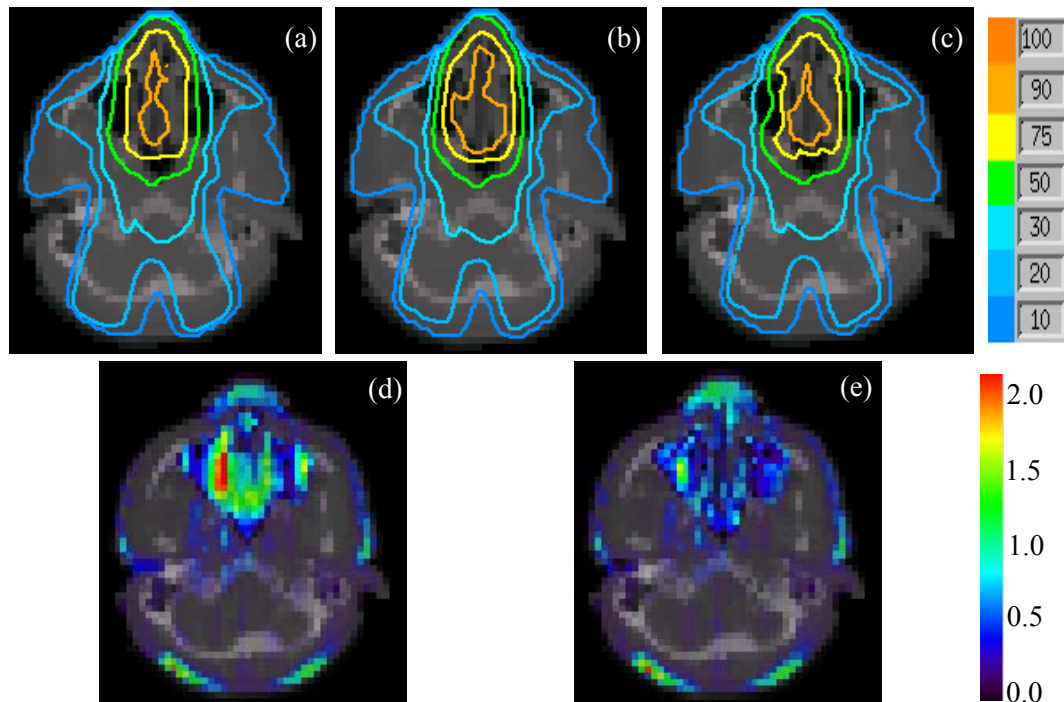


**Figure 1.** Dose distributions for Case H3 calculated with the MCSIM (a), g-FSPB (b), and g-DC-FSPB (c) algorithms in the XY plane through the isocenter. The  $\gamma$ -index distributions are shown in (d) for g-FSPB and (e) for g-DC-FSPB dose distributions in the same plane.

280



281 *Scenario 3 (Case H4 and Case H5) - both g-FSPB and g-DC-FSPB algorithms are*  
 282 *less accurate. For these two cases, the g-FSPB dose distributions have large average  $\gamma$ -*  
 283 *index values ( $\gamma_{50}^{avg} \sim 0.6$ ) and low passing rates ( $P_{50} \sim 86\%$ ). With 3D density correction,*  
 284 *the accuracy of the dose distributions is not much improved. By carefully inspecting*  
 285 *these two cases, we found that in both cases there are dental fillings of very high density*  
 286 *( $\sim 4.0 \text{ g/cm}^3$ ). Figure 2(a) shows dose distribution calculated with the g-DC-FSPB*  
 287 *algorithm and the density map of Case H4 in the XY plane through the isocenter, in*  
 288 *which we can clearly see the high density dental fillings. The dose difference maps*  
 289 *between the MCSIM and g-DC-FSPB dose distributions for each of the 5 co-planar*  
 290 *beams ( $309^\circ$ ,  $0^\circ$ ,  $51^\circ$ ,  $102^\circ$ , and  $153^\circ$ ) are illustrated in Figures 2 (b)-(f). We can see that*  
 291 *the beam at angle  $309^\circ$  passes through the high density dental filling region before hitting*  
 292 *the target, causing a dose discrepancy up to 8% of  $D_{max}$  between the g-DC-FSPB and*  
 293 *MCSIM results. This is because the density values near  $4.0 \text{ g/cm}^3$  are far beyond our*  
 294 *commissioned density range and thus the g-DC-FSPB algorithm cannot find proper*  
 295 *parameters to accurately calculate the dose. For the other four beams, since they do not*  
 296 *pass through the high density region, the g-DC-FSPB dose distributions agree well*  
 297 *(within 1-2% of  $D_{max}$ ) with the MCSIM dose distributions.*

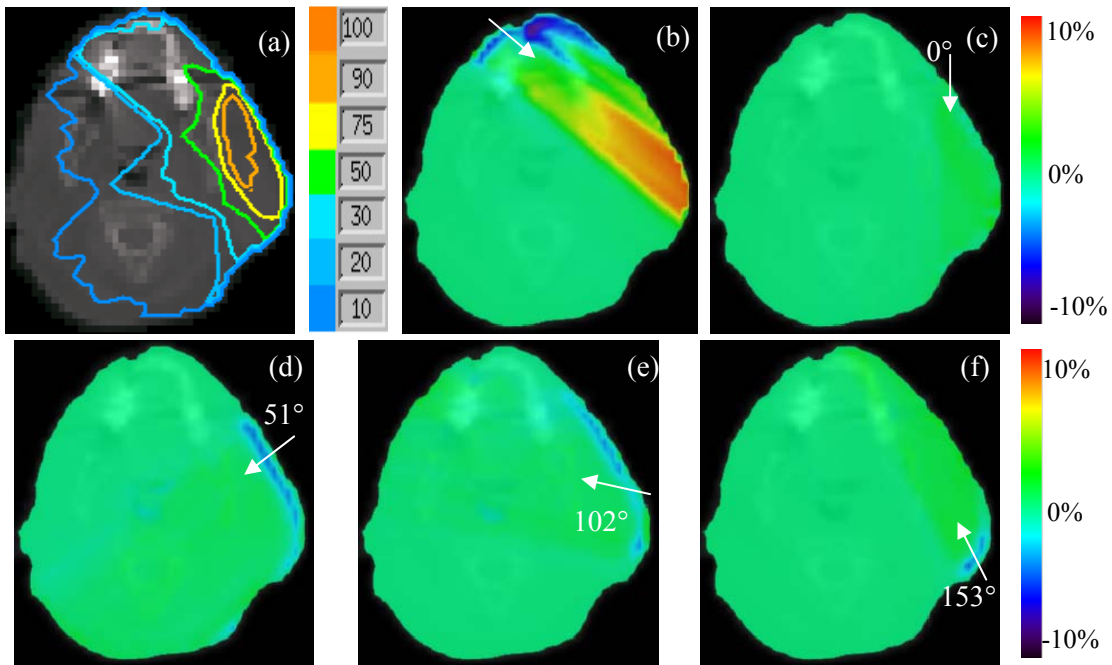


**Figure 2.** (a) Dose distributions for Case H4 calculated with the g-DC-FSPB algorithm in the XY plane through the isocenter. The dose difference maps in the unit of  $\% D_{max}$  between the g-DC-FSPB and the MCSIM results are shown in the same plane for each individual beam at the angle: (b)  $309^\circ$ , (c)  $0^\circ$ , (d)  $51^\circ$ , (e)  $102^\circ$ , and (f)  $153^\circ$ .

298

### 299 3.1.2 Lung cases

300

301 In Case L1, the tumor site is located in the lower lobe of the left lung, closing to the  
 302 pleura. The 5 out of total 6 beams do not pass through low-density lung regions before  
 303 hitting the target, in which cases the g-FSPB algorithm has sufficient accuracy. The last

304 beam goes through the low-density lung regions to reach the target and thus the 3D  
 305 density correction is needed to achieve high accuracy. The combined effect of all 6  
 306 beams is that, using the g-DC-FSPB method,  $\gamma_{50}^{avg}$  is reduced from 0.45 to 0.24 and  $P_{50}$   
 307 is increased from 94.81% to 99.35%.  
 308

**Table 3.** Gamma index evaluation results for 5 lung cases using the g-DC-FSPB algorithm.  
 The corresponding g-FSPB results are given in parenthesis for comparison purpose.

Case #	$\gamma^{max}$	$\gamma_{50}^{avg}$	$P_{50}$
L1	1.53 (1.92)	0.24 (0.45)	99.35% (94.81%)
L2	2.35 (3.30)	0.36 (0.71)	96.64% (76.38%)
L3	1.68 (3.07)	0.32 (0.75)	99.16% (76.60%)
L4	2.70 (4.59)	0.63 (1.53)	81.33% (28.55%)
L5	2.19 (4.34)	0.49 (1.13)	90.24% (57.03%)

309 In Case L2, the tumor site is close to the vertebral body. Three out of six beams strike  
 310 the targets without passing through low-density lung regions. For these beams the g-  
 311 FSPB algorithm can generate accurate results. For the other three beams, which pass  
 312 through lung areas before hitting the target, the g-FSPB algorithm becomes inadequate.  
 313 The dose distributions calculated with the MCSIM, g-FSPB and g-DC-FSPB algorithms  
 314 are plotted in the XY plane through isocenter in Figures 3(a), 3(b), and 3(c). In Figure  
 315 3(b), the g-FSPB dose is much higher than the MCSIM dose in the region indicated by  
 316 the arrow. When the g-DC-FSPB algorithm is used, this hot spot disappears, as shown in  
 317 Figure 3(c). Figures 3(d) and 3(e) plot the  $\gamma$ -index distributions in the same plane  
 318 calculated with the g-FSPB and g-DC-FSPB algorithms, respectively. The statistical  
 319 values shown in Table 3 also indicate a significant improvement of  $\gamma_{50}^{avg}$  and  $P_{50}$  values  
 320 using the 3D density correction method, where,  $\gamma_{50}^{avg}$  values decrease from 0.71 to 0.36  
 321 and  $P_{50}$  values increase from 76.38% to 96.64%. The situation for Case L3 is very similar  
 322 to that of Case L2.

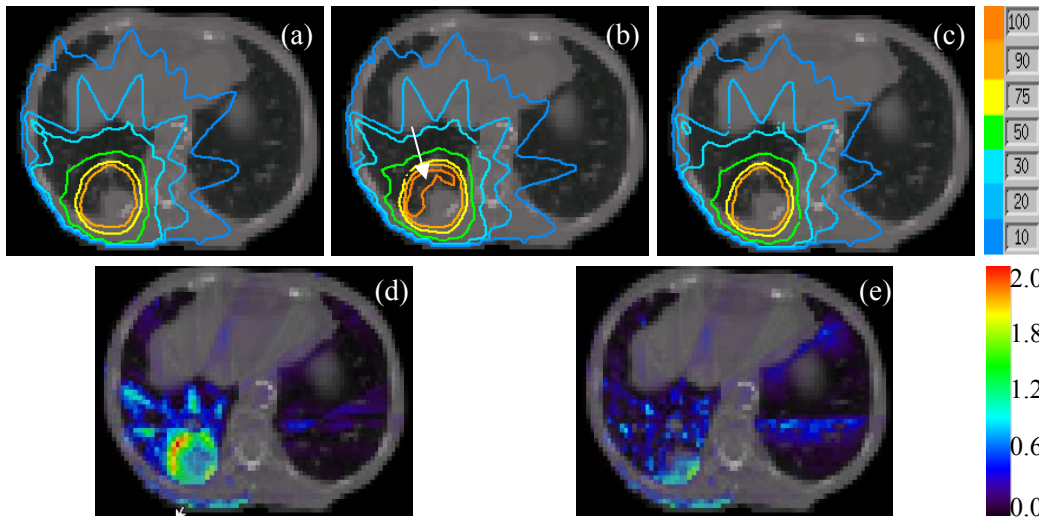


**Figure 3.** The dose distribution of Case L2 calculated with MCSIM (a), g-FSPB (b), and g-DC-FSPB (c) in the XY plane through the isocenter. The  $\gamma$ -index distributions in the same plane are illustrated in (d) for g-FSPB and (e) for g-DC-FSPB.

323 The tumor in Case L4 is in the middle of the lung, indicating that all beams have to  
 324 pass through the low-density lung regions before hitting the target. The dose distributions  
 325 in the XY plane through isocenter calculated with the MCSIM, g-FSPB and g-DC-FSPB  
 326 algorithms are shown in Figures 4(a), (b), and (c). The  $\gamma$ -index distributions in the same  
 327 plane calculated with the g-FSPB and g-DC-FSPB algorithms are plotted in Figures 4(d)  
 328 and (e). From Figures 4(a), 4(b), and 4(d), we observe that in the high dose region, the g-  
 329 FSPB algorithm heavily overestimates the calculated dose. From Figures 4(c) and 4(e),  
 330 we can see that the g-DC-FSPB algorithm can correct the overestimation of the g-FSPB  
 331 algorithm and greatly improve the agreement with MCSIM, especially inside the target  
 332 region. However, in lung regions outside the target, the density correction is overdone,  
 333 resulting in an underestimated dose.

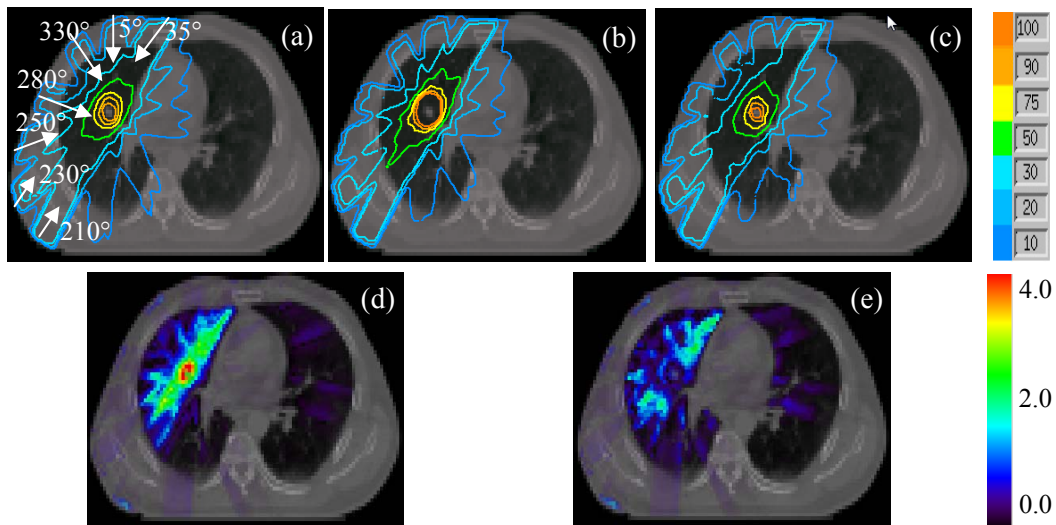


**Figure 4.** Dose distributions for Case L4 in the XY plane through the isocenter calculated with the MCSIM (a), g-FSPB (b), and g-DC-FSPB (c) algorithms.  $\gamma$ -index distributions for the g-FSPB (d) and g-DC-FSPB (e) algorithms are given in the same plane.

334

335 The dose distribution for Case L4 is analyzed individually for each of the 7 coplanar  
 336 beams at the gantry angles of 35°, 5°, 330°, 280°, 250°, 230°, and 210°. In Figures 5, we  
 337 plot the normalized depth dose curves and depth density curves for each beam. Here, we  
 338 normalize three depth dose curves for each beam to the maximum dose calculated with  
 339 MCSIM algorithm for that beam. We can see that, without 3D-density correction, all the  
 340 depth dose curves exhibit a monotonic decrease after the maximum dose and do not show  
 341 a clear inhomogeneity correction effect. In contrast, the depth dose curves calculated with  
 342 the g-DC-FSPB algorithm exhibit a proper trend of density correction, *i.e.*, build-down  
 343 and build-up effects, as indicated by the MCSIM depth dose curves. Overall, the  
 344 calculated dose distribution of each beam is significantly improved with 3D-density  
 345 correction. For the composite dose distribution, as shown in Table 3, the  $\gamma$ -index passing  
 346 rate inside 50% isodose line has been improved from 28.55% to 81.33%. However, for  
 347 some beams the g-DC-FSPB algorithm overcorrects the density effect, leading to a much  
 348 underestimated dose in lung regions. This phenomenon is particularly obvious for gantry

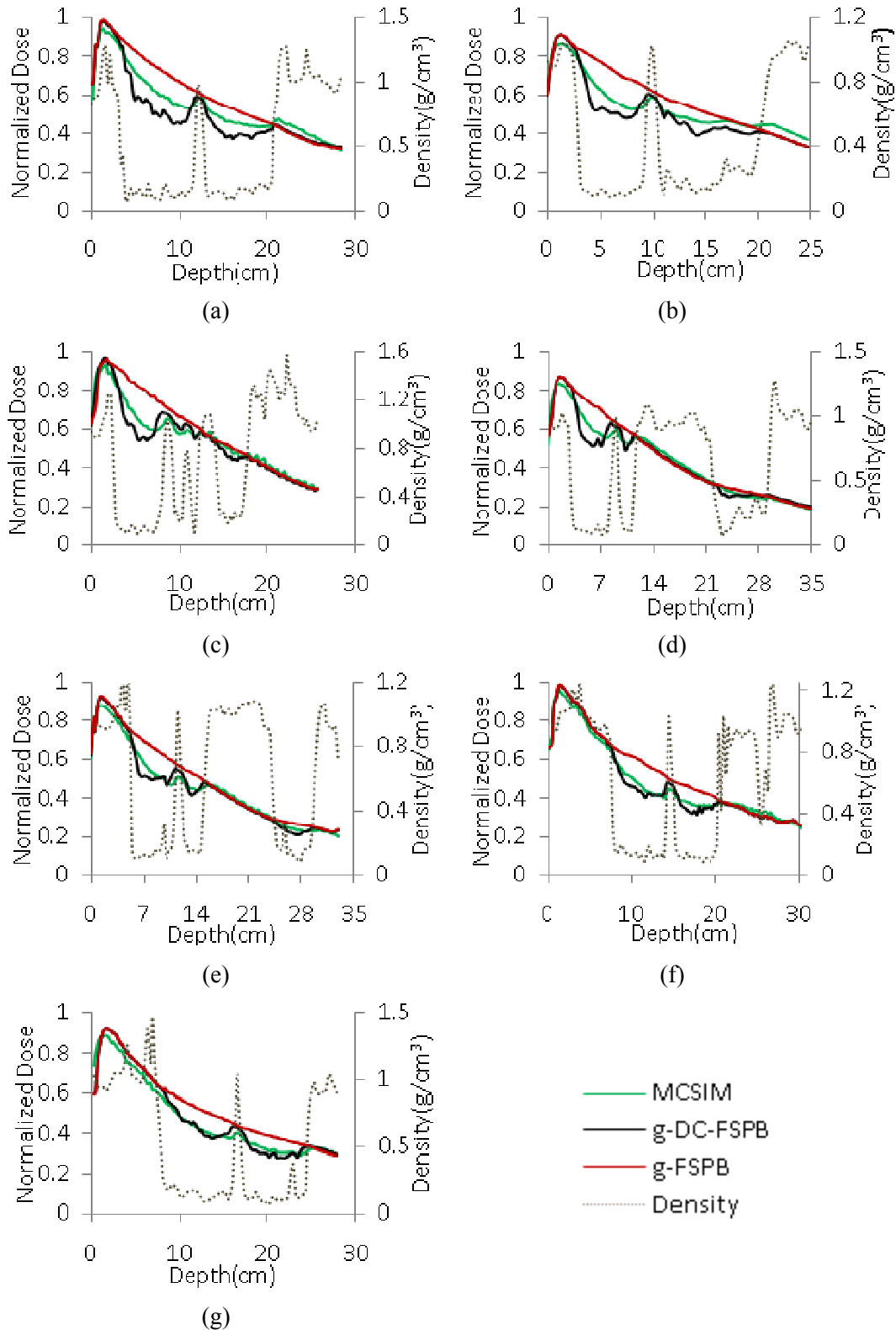


**Figure 5.** The depth dose curves and the depth density curves along the beam central axis for seven beams (a) 35°, (b) 5°, (c) 330°, (d) 280°, (e) 250°, (f) 230°, and (g) 210°. The depth dose curves are normalized to each beam's maximum dose calculated with MCSIM.

349 angle such 35°, which is mainly responsible for the discrepancy shown in Figure 4(e).  
 350 Similarly, for Case L5, the improvement of dose distribution achieved by the 3D-density  
 351 correction method is dramatic. However the  $\gamma$ -index passing rate in the 50% isodose line  
 352 for the g-DC-FSPB algorithm is still less satisfactory due to the similar overcorrection  
 353 issue.

354

### 355 3.2 Efficiency evaluation

356

357 Table 4 lists computation time for dose calculation using the g-FSPB and g-DC-FSPB  
 358 algorithms. We can see that the dose distribution of a realistic IMRT plan can be  
 359 computed at a very high efficiency. For 9 out of 10 testing cases, the dose calculation can  
 360 be completed within one second using either algorithm. For all 10 cases, the median data  
 361 transfer time between CPU and GPU is 0.2 seconds, and the median GPU computation  
 362 time is 0.37 seconds for the g-DC-FSPB algorithm and 0.33 seconds for the g-FSPB  
 363 algorithm. Since the computation time is so short, the data transfer time takes a  
 364 significant portion of the total computation time, up to 50% in Case L1. We can also see  
 365 that, while the accuracy of the g-DC-FSPB algorithm is much higher than that of the g-  
 366 FSPB algorithm, its efficiency sacrifice is quite mild (~5-15% slower in terms of the total  
 367 computation time).

368

**Table 4.** Dose calculation time using the g-FSPB (in parenthesis) and g-DC-FSPB algorithms for 10 testing cases.  $T_{tr}$  is the data transfer time between CPU and GPU.  $T_{gpu}$  is the GPU computation time.  $T_{tot} = T_{tr} + T_{gpu}$ .

Case #	$T_{tr}(\text{sec})$	$T_{gpu}(\text{sec})$	$T_{tot}(\text{sec})$
H1	0.20	0.64 (0.55)	0.84 (0.75)
H2	0.20	0.40 (0.35)	0.60 (0.55)
H3	0.20	0.38 (0.34)	0.58 (0.54)
H4	0.19	0.35 (0.32)	0.54 (0.51)
H5	0.20	1.31 (1.10)	1.51 (1.30)
L1	0.21	0.22 (0.20)	0.43 (0.41)
L2	0.22	0.40 (0.36)	0.62 (0.58)
L3	0.21	0.30 (0.25)	0.51 (0.46)
L4	0.18	0.25 (0.23)	0.43 (0.41)
L5	0.21	0.33 (0.29)	0.54 (0.50)
Median	0.20	0.37 (0.33)	0.56 (0.53)

369

## 370 4. Conclusions

371

372 In this paper, we detailed the implementation of the g-DC-FSPB algorithm. The  
 373 dosimetric evaluation of the g-DC-FSPB algorithm was conducted on 5 head-and-neck  
 374 and 5 lung IMRT treatment plans. Using the dose distributions computed with the  
 375 MCSIM Monte Carlo code as reference, we assessed the accuracy improvement of the g-  
 376 DC-FSPB algorithm over the g-FSPB algorithm.

377 For head and neck cases, 1) when only minor heterogeneities exist, the g-FSPB  
378 algorithm is already quite accurate and the improvement achieved by the g-DC-FSPB  
379 algorithm is mild; 2) when air cavities are near the target, the g-DC-FSPB algorithm can  
380 significantly improve the accuracy of dose distribution; 3) when there are high-density  
381 dental filling materials in the beam paths, the dose calculation accuracy of the g-DC-  
382 FSPB algorithm is unsatisfactory although there is still an improvement over the g-FSPB  
383 algorithm, due to the fact that such high-density materials were not considered in the  
384 commissioning process.

385 For all lung cases, the accuracy of calculated dose distributions is significantly  
386 improved with the 3D-density correction method. However, the degree of such  
387 improvement is highly dependent on inhomogeneities presented in the beam paths. When  
388 the majority of beams in a treatment plan reach the target without passing through the  
389 low-density lung region, the accuracy of dose distribution calculated by the g-FSPB  
390 algorithm is already satisfactory, while there is still a significant improvement with the  
391 3D-density correction method. When more than half of the beams in a treatment plan  
392 have to pass through the low-density lung region before reaching the target, the accuracy  
393 of the g-FSPB algorithm is poor, while the g-DC-FSPB algorithm can dramatically  
394 improve the dose calculation accuracy.

395 In the original work of Jelen *et al.* (2007), better than 2% of accuracy was  
396 demonstrated for the majority of the voxels inside the field when using the DC-FSPB  
397 model, which seems better than our g-DC-FSPM algorithm. We would like to point out  
398 that their accuracy was accomplished for a single flat  $10 \times 10\text{cm}^2$  beam in a lung case  
399 and a  $6 \times 6\text{cm}^2$  beam in a head-and-neck case, while our results were obtained for 10  
400 real clinical IMRT cases.

401 Regarding the efficiency, we see that for 9 out of 10 testing cases, the dose  
402 calculation can be completed well within one second for both g-FSPB and g-DC-FSPB  
403 algorithms. The median GPU computation times are less than half a second for both  
404 algorithms. Compared to the g-FSPB algorithm, the g-DC-FSPB algorithm slightly  
405 sacrifices the computation efficiency, about 5-15% slower in terms of the total  
406 computation time. However, the significant accuracy improvement of the g-DC-FSPB  
407 algorithm far outweighs the slight efficiency lost, indicating that this algorithm is more  
408 suitable for online IMRT replanning.

409

#### 410 **Acknowledgements**

411

412 This work is supported in part by the University of California Lab Fees Research  
413 Program and by an NIH/NCI grants 1F32 CA154045-01. We would like to thank  
414 NVIDIA for providing GPU cards for this project.

415

416 **Reference**

417

- 418 Ahunbay E E, Peng C, Chen G P, Narayanan S, Yu C, Lawton C and Li X A 2008 An  
419 on-line replanning scheme for interfractional variations *Medical Physics* **35**  
420 3607-15
- 421 Ahunbay E E, Peng C, Holmes S, Godley A, Lawton C and Li X A 2010 ONLINE  
422 ADAPTIVE REPLANNING METHOD FOR PROSTATE RADIOTHERAPY  
423 *International Journal of Radiation Oncology Biology Physics* **77** 1561-72
- 424 Court L E, Dong L, Lee A K, Cheung R, Bonnen M D, O'Daniel J, Wang H, Mohan R  
425 and Kuban D 2005 An automatic CT-guided adaptive radiation therapy technique  
426 by online modification of multileaf collimator leaf positions for prostate cancer  
427 *International Journal of Radiation Oncology Biology Physics* **62** 154-63
- 428 Court L E, Tishler R B, Petit J, Cormack R and Chin L 2006 Automatic online adaptive  
429 radiation therapy techniques for targets with significant shape change: a  
430 feasibility study *Phys. Med. Biol.* **51** 2493-501
- 431 Fippel M, Laub W, Huber B and Nusslin F 1999 XVMC-fast Monte-Carlo dose  
432 calculation for photon beam treatment planning *Z. Med. Phys.* 255-60
- 433 Fu W H, Yang Y, Yue N J, Heron D E and Huq M S 2009 A cone beam CT-guided  
434 online plan modification technique to correct interfractional anatomic changes  
435 for prostate cancer IMRT treatment *Phys. Med. Biol.* **54** 1691-703
- 436 Godley A, Ahunbay E, Peng C and Li X A 2009 Automated registration of large  
437 deformations for adaptive radiation therapy of prostate cancer *Medical Physics*  
438 **36** 1433-41
- 439 Gu X J, Choi D J, Men C H, Pan H, Majumdar A and Jiang S B 2009 GPU-based ultra-  
440 fast dose calculation using a finite size pencil beam model *Phys. Med. Biol.* **54**  
441 6287-97
- 442 Gu X J, Jia X and Jiang S B 2010a GPU-based fast gamma index calculation *submitted to*  
443 *Physics in Medicine and Biology*
- 444 Gu X J, Pan H, Liang Y, Castillo R, Yang D S, Choi D J, Castillo E, Majumdar A,  
445 Guerrero T and Jiang S B 2010b Implementation and evaluation of various  
446 demons deformable image registration algorithms on a GPU *Phys. Med. Biol.* **55**  
447 207-19
- 448 Hissoiny S, Ozell B and Despres P 2009 Fast convolution-superposition dose calculation  
449 on graphics hardware *Medical Physics* **36** 1998-2005
- 450 Hissoiny S, Ozell B and Despres P 2010 A convolution-superposition dose calculation  
451 engine for GPUs *Medical Physics* **37** 1029-37
- 452 Jacques R, Taylor R, Wong J and McNutt T 2010 Towards real-time radiation therapy:  
453 GPU accelerated superposition/convolution *Comput. Meth. Programs Biomed.* **98**  
454 285-92
- 455 Jelen U and Alber M 2007 A finite size pencil beam algorithm for IMRT dose  
456 optimization: density corrections *Phys. Med. Biol.* **52** 617-33
- 457 Jelen U, Sohn M and Alber M 2005 A finite size pencil beam for IMRT dose  
458 optimization *Phys. Med. Biol.* **50** 1747-66
- 459 Jia X, Gu X J, Sempau J, Choi D, Majumdar A and Jiang S B 2010a Development of a  
460 GPU-based Monte Carlo dose calculation code for coupled electron-photon  
461 transport *Phys. Med. Biol.* **55** 3077-86
- 462 Jia X, Lou Y F, Li R J, Song W Y and Jiang S B 2010b GPU-based fast cone beam CT  
463 reconstruction from undersampled and noisy projection data via total variation  
464 *Medical Physics* **37** 1757-60
- 465 Jiang S B, Deng J, Li J S, Pawlicki T, Boyer A L and Ma C-M 2000 Modeling and  
466 Commissioning of Clinical Photon Beams for Monte Carlo Treatment Planning.

- 467 In: *Proc. of the 13th International Conference on the Use of Computer in*  
468 *Radiation Therapy (ICCR)*, , ed W Schlegel and T Bortfeld (Heidelberg:  
469 Springer-Verlag) pp 434-6
- 470 Li G, Xie H C, Ning H, Citrin D, Capala J, Maass-Moreno R, Guion P, Arora B,  
471 Coleman N, Camphausen K and Miller R W 2008 Accuracy of 3D volumetric  
472 image registration based on CT, MR and PET/CT phantom experiments *Journal*  
473 *of Applied Clinical Medical Physics* **9** 17-36
- 474 Lu W G 2010 A non-voxel-based broad-beam (NVBB) framework for IMRT treatment  
475 planning *Phys. Med. Biol.* **55** 7175-210
- 476 Lu W G, Chen M, Chen Q, Ruchala K and Olivera G 2008 Adaptive fractionation  
477 therapy: I. Basic concept and strategy *Phys. Med. Biol.* **53** 5495-511
- 478 Lu W G and Chen M L 2010 Fluence-convolution broad-beam (FCBB) dose calculation  
479 *Phys. Med. Biol.* **55** 7211-29
- 480 Ma C-M, Li J S, Pawlicki T, Jiang S B, Deng J, Lee M C, Koumrian T, Luxton M and  
481 Brain S 2002 A Monte Carlo dose calculation tool for radiotherapy treatment  
482 planning *Phys. Med. Biol.* **47** 1671
- 483 Men C H, Gu X J, Choi D J, Majumdar A, Zheng Z Y, Mueller K and Jiang S B 2009  
484 GPU-based ultrafast IMRT plan optimization *Phys. Med. Biol.* **54** 6565-73
- 485 Men C H, Jia X and Jiang S B 2010a GPU-based ultra-fast direct aperture optimization  
486 for online adaptive radiation therapy *Phys. Med. Biol.* **55** 4309-19
- 487 Men C H, Jia X, Jiang S B and Romeijn H E 2010b Ultrafast treatment plan optimization  
488 for volumetric modulated arc therapy (VMAT) *Medical Physics* **37** 5787-91
- 489 Mohan R, Zhang X D, Wang H, Kang Y X, Wang X C, Liu H, Ang K, Kuban D and  
490 Dong L 2005 Use of deformed intensity distributions for on-line modification of  
491 image-guided IMRT to account for interfractional anatomic changes  
492 *International Journal of Radiation Oncology Biology Physics* **61** 1258-66
- 493 NVIDIA 2010 NVIDIA CUDA Compute Unified Device Architecture, Programming  
494 Guide version 3.2. ed NVIDIA
- 495 Samant S S, Xia J Y, Muyan-Ozcelilk P and Owens J D 2008 High performance  
496 computing for deformable image registration: Towards a new paradigm in  
497 adaptive radiotherapy *Medical Physics* **35** 3546-53
- 498 Sharp G C, Kandasamy N, Singh H and Folkert M 2007 GPU-based streaming  
499 architectures for fast cone-beam CT image reconstruction and demons  
500 deformable registration *Phys. Med. Biol.* **52** 5771-83
- 501 Siddon R L 1985 Fast calculation of the exact radiological path for a 3-dimensional CT  
502 array *Medical Physics* **12** 252-5
- 503 Wu C, Jeraj R, Lu W G and Mackie T R 2004 Fast treatment plan modification with an  
504 over-relaxed Cimmino algorithm *Medical Physics* **31** 191-200
- 505 Wu C, Jeraj R, Olivera G H and Mackie T R 2002 Re-optimization in adaptive  
506 radiotherapy *Phys. Med. Biol.* **47** 3181-95
- 507 Wu Q J, Thongphiew D, Wang Z, Mathayomchan B, Chankong V, Yoo S, Lee W R and  
508 Yin F F 2008 On-line re-optimization of prostate IMRT plans for adaptive  
509 radiation therapy *Phys. Med. Biol.* **53** 673-91
- 510 Yan H, Ren L, Godfrey D J and Yin F F 2007 Accelerating reconstruction of reference  
511 digital tomosynthesis using graphics hardware *Medical Physics* **34** 3768-76
- 512
- 513